Journal of Vibration and Control
XX(X):1–14

DOI: 10.1177/ToBeAssigned
www.sagepub.com/
SAGE

The role of evanescent modes in Global-Local analysis of UGW in plates with varying local zone-scatterer relations

Antonino Spada[1], Mingyue Zhang[2], Francesco Lanza di Scalea[3] and Margherita Capriotti[2]

Abstract

In order to provide a reliable and robust SHM performance, Ultrasonic Guided Waves (UGWs) need to be analyzed and understood. Numerical modeling of UGW propagation and scattering by hybrid methods offers the possibility of simulating UGW interaction with waveguides of arbitrary cross-sections and discontinuities. Maximizing the accuracy of such methods is important to perform quantitative SHM, while maintaining minimum computational cost.

This work investigates the role of evanescent modes in the numerical analysis of UGWs in aluminum and composite plates with defects, by the hybrid Global-Local method. The complex solutions to the UGW eigenvalue problem are found and the scattering spectra for A0 and S0 incident modes are calculated. The accuracy of the numerical solution is then studied by computing the error in terms of energy balance.

Parametric studies with respect to the local zone size, defect dimensions and shape are conducted including and excluding evanescent modes in the analysis. Considerations are provided to obtain a solution with error no greater than 5%, in terms of varying local zone – scatterer relations within plate waveguides.

Keywords

evanescent modes, numerical modeling, scattering, defect, Ultrasonic Guided Waves, Structural Health Monitoring

Introduction

In the last decades, the use of ultrasonic guided waves (UGWs) has increased considerably for NDE and SHM purposes, in a variety of materials, geometries and applications. This is due to the potential that UGWs offer in terms of long-range propagation, cross-sectional involvement and sensitivity to defects (Staszewski (2004)). In order to provide a reliable and robust SHM performance, UGW propagation and scattering have to be analyzed and understood in detail (Willberg et al. (2015)). While analytical solutions are available for waveguides of uniform cross-section and in cases where discontinuities or defects are easily defined by boundary conditions, numerical methods are required to solve UGW propagation problems in waveguides of arbitrary cross-section and/or in the presence of more complex structural configurations, materials or defects. Moreover, numerical simulations allow for the study of a large number of cases and variables to account for, that would be cumbersome or nearly impossible to observe experimentally.

To date, a wide range of numerical methods have been employed to model UGW propagation and scattering: a review in 2015 (Willberg et al. (2015)) describes the main strategies, also emphasizing each method's advantages and disadvantages. Although finite element methods (FEM) are still heavily used as benchmark for the comparison of reduced-order and other approximation methods (Leckey et al. (2018)), and for the design and interpretation of experimental results, particularly in cases of complex damages (Ricci et al. (2016)), and structures (Gavrić (1995)), they are computationally expensive, require extensive efforts to interpret the spectral content of the waveform and do not allow mode excitability and sensitivity studies. This is even more relevant when a broadband frequency analysis is required. Among others (finite difference (Lee and Staszewski (2003); Frankforter et al. (2019)), spectral elements (Ostachowicz et al. (2011), boundary element, etc.), the Semi Analytical Finite Elements method (SAFE) enables to model UGW propagation in cross-sections of arbitrary geometry and varying material properties. This is achieved by discretizing the cross-section with FE. An eigenvalue problem is then posed to solve for the complex wavenumber and wavemodes, that are then propagated analytically, in the wave propagation direction (Hayashi et al. (2003); Bartoli et al. (2006); Marzani et al. (2008)). To include scattering and wave propagation from the UGW interaction with geometrical discontinuities, damages and any changes along the wave propagation direction, the SAFE method needs to be coupled with

[1]Department of Engineering, University of Palermo, Viale delle Scienze, Ed. 8, 90128, Palermo, Italy.
[2]Aerospace Engineering Department, San Diego State University, 5500 Campanile Dr., 92182, San Diego, CA, USA.
[3]Experimental Mechanics & NDE Laboratory, Department of Structural Engineering, University of California San Diego, 9500 Gilman Drive, La Jolla, CA 92093-0085, USA.

Corresponding author:
Prof. Antonino Spada, Department of Engineering, University of Palermo, Viale delle Scienze, Ed. 8, 90128, Palermo, Italy.
Email: antonino.spada@unipa.it

other computational approaches (hybrid methods). Mal and Chang (2000) first proposed this hybrid method to calculate the elastodynamic field in a plate containing geometric discontinuities. Srivastava and Lanza di Scalea (2010) presented the so-called Global-Local (GL) method, a hybrid SAFE-FE method, for quantitative SHM in multilayered structures with defects.

The validation and accuracy of numerical methods is of crucial importance to enable quantitative and robust SHM. While validation is performed by comparing simulation results with analytical solutions and experimental data (when available) and FEM results of the reproduced case study, the evaluation of accuracy has been commonly addressed by the computation of an energy balance.

Moreover, the complexity of UGW scattering is increased also by the presence of propagating and non-propagating modes. This aspect is of particular importance when the contribution of near-field effects cannot be neglected, such as in the presences of free ends and in the vicinity of waveguide or defect edges. Gazis and Mindlin (1960) studied complex roots in the analytical solution of waves propagating in plates with respect to edge modes and plate thickness over distance ratio, and compared the zeroth and second order theory. Using the SAFE method, Taweel et al. (2000) studied the effect of propagating and non-propagating modes on the energy balance in free ends of a bar or cylinder with respect to the height over width ratio: it was found that different solution methods require a different number of modes to satisfy energy balance. Later, Bartoli et al. (2006) studied UGWs propagation in damped and undamped waveguides of isotropic and composite materials with the SAFE method, including evanescent modes. Another research group used the modal decomposition method to study S0 and A0 mode scattering from perpendicular cracks and free end of plates (Castaings et al. (2002); Diligent et al. (2003)). The effect of evanescent modes was here evaluated and it was concluded that, although the power flow has to be computed only for incident and scattered propagative modes, the energy balance must include complex (evanescent) modes to satisfy boundary conditions, hence to obtain an accurate solution. 3D UGWs scattering by through thickness cavities of irregular shapes was studied analytically by the use of normal Lamb waves (propagating and evanescent) by Moreau et al. (2011): energy balance was computed to evaluate the convergence error with respect to the number of modes to be included, for different incident modes and defect aspect ratios. A similar method (CMEP) was more recently used by Poddar and Giurgiutiu (2016) in 2D aluminum plates with horizontal cracks: a convergence analysis was performed to assess the number of complex roots to be included for an accurate solution. Also, Schaal et al. (2017) studied UGW propagation in the case of scattering from horizontal cracks in an aluminum plate, using the WFE (Wave FE) method: complex roots where included to account for the near field effects in leading and trailing edges of the crack and conservation of power flow was evaluated to calculate error.

In the case of scattering in complex waveguide cross-sections and defects, such as in railroad tracks, a hybrid method (spectral super element coupled to FE) is used (Ryue et al. (2011)): complex solutions are here included and error is evaluated in terms of conservation of the incident energy. Using a similar concept (WFE coupled to FE) Zhou and Ichchou (2011) studied the effect of defect size on UGWs scattering in plates, including evanescent modes and a forced formulation to compute time-domain scattered waveforms. A hybrid method (SAFE coupled to FE) was also used by Benmeddour et al. (2011) to validate the method for UGWs scattering at free ends and vertical discontinuities of cylindrical waveguides: the number of non-propagating modes to be included in the analysis for an accurate result was decided depending on the magnitude of the imaginary part of the product wavenumber and radius.

In this paper, the authors study the role of evanescent modes in the accurate modeling of UGWs scattering in isotropic and composite plate waveguides, with respect to defect shapes and sizes. The hybrid GL method, expanded by the authors and applied on complex composite structures and 3D geometries (Spada et al. (2020); Spada et al. (2022)), is here used and its accuracy is assessed through energy balance to provide considerations in terms of the local FE zone and scatterer relation.

Theoretical Formulation

The GL method formulates the UGW propagation problem by identifying two regions in the complex waveguide (Fig. 1): the local region contains any discontinuity and/or structural defect, and the global region represents an infinite waveguide of arbitrary cross-section. The formulation is here briefly presented in 2D. A detailed formulation can be found in Spada et al. (2020). An incident time-harmonic guided wave excited in the sound (global) region propagates along the wave propagation direction and is scattered into reflected and transmitted waves, after interacting with the discontinuity within the local region. The equilibrium of each region is guaranteed by imposing the Principle of Virtual Work (PVW).

SAFE Solution

The cross-section (thickness in the 2D case) of the waveguide in the global (g) region is discretized by FE and a harmonic exponential term $e^{i(\xi x-\omega t)}$ describes the analytical wave propagation, to obtain nodal displacements, strains and stresses, where ξ is the wavenumber and ω is the angular frequency. The stiffness matrix $\mathbf{K}^g$, mass matrix $\mathbf{M}^g$ and force vector $\mathbf{F}^g$ are computed for the global region and the PVW is applied, obtaining:

$$(\mathbf{K}^g - \omega^2\mathbf{M}^g)\mathbf{U}^g = \mathbf{F}^g \tag{1}$$

where in the case of an unforced solution the right-side of Eq. (1) is 0. This reduces to an eigenvalue problem where the wavenumbers ξ and wavemodes ϕ can be found in terms of eigenvalues and eigenvectors. The eigenvalues can be pairs of real, complex and imaginary numbers, representing propagating, evanescent decaying and evanescent non-oscillating (end-modes) waves, respectively. Following Benmeddour et al. (2011), a threshold equal to $Im(\xi h) = [-5, 5]$ has been placed to select the evanescent modes, where h is the thickness of the waveguide. A total of N_M modes is found as the sum of propagating

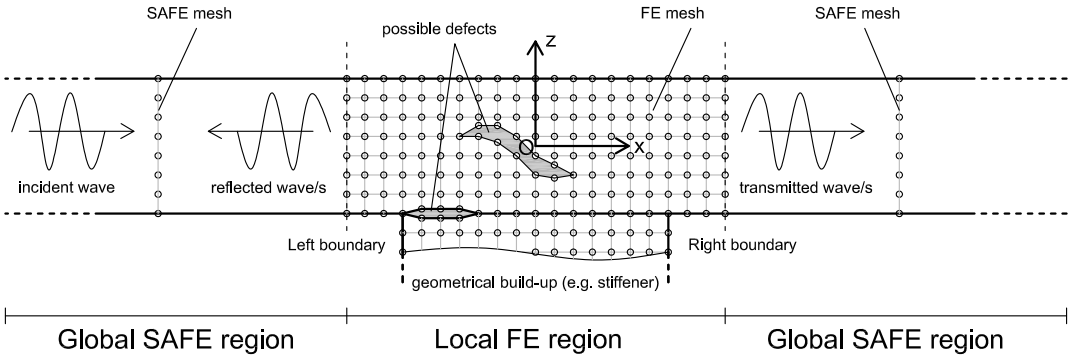

Figure 1. Geometrical representation of the scattering of an incident wave in reflected and transmitted waves from a local region, with indication of the adopted discretization strategies in each region of the Global-Local approach.

and evanescent modes. Phase and group velocity are then computed as $c_p = \omega/\xi_{Re}$ and $c_g = \frac{\partial\omega}{\partial\xi}$, as well as attenuation $att = \xi_{Im}$ and energy velocity $c_{En} = \frac{\frac{1}{\Gamma}\int_\Gamma \boldsymbol{P}\cdot\boldsymbol{n}d\Gamma}{\frac{1}{T}\int_T(\frac{1}{\Gamma}\int_\Gamma e_{tot}d\Gamma)dt}$, where Γ is the cross-sectional area, $\boldsymbol{P}$ is the Poynting vector (real part only), $\boldsymbol{n}$ is the propagation direction unit vector, e_{tot} is the total energy density (kinetic and potential), T is the period.

Coupled Global-Local Solution

The nodal displacements at the left boundary $\boldsymbol{q}_{lB}$ of the local region are the combination of the incident wave and the reflected waves, while those at the right boundary $\boldsymbol{q}_{rB}$ are a combination of the transmitted ones:

$$\boldsymbol{q}_{lB} = \boldsymbol{q}_{in} + \boldsymbol{q}_{Refl}; \tag{2}$$

$$\boldsymbol{q}_{rB} = \boldsymbol{q}_{Transm}. \tag{3}$$

In the case of UGW propagation and scattering, the incident, reflected and transmitted waves can be thought of as the superposition of weighted N_M wavemodes, corresponding to the global cross-sectional modeshapes obtained in the SAFE solution:

$$\boldsymbol{q}_{lB} = \boldsymbol{\Phi}^+_{in} e^{i[\xi^+_{in}(x_S - x_{lB})]} + \sum_{j=1}^{N_M} A^-_j \boldsymbol{\Phi}^{(j)^-} e^{i(\xi^-_j x_{lB})}; \tag{4}$$

$$\boldsymbol{q}_{rB} = \sum_{j=1}^{N_M} A^+_j \boldsymbol{\Phi}^{(j)^+} e^{i(\xi^+_j x_{rB})}. \tag{5}$$

The weights are the amplitude A_j of the modeshapes, which are calculated by least square method on the system:

$$\boldsymbol{S}\,\boldsymbol{U}^l = \boldsymbol{F}^l \tag{6}$$

where $\boldsymbol{S}$ is the dynamic stiffness matrix for the local region, $\boldsymbol{U}^l$ and $\boldsymbol{F}^l$ are the vectors containing the nodal displacements and forces for the local region, including those at the left and right boundary.
Such amplitudes represent the scattering (reflected and transmitted) coefficients.

Energy Balance

Once the amplitudes are determined, the energy carried by each j-th mode can be calculated as:

$$E^j = -\frac{|A_j|^2}{2} Re[i\omega \boldsymbol{F}^{j^T} \bar{\boldsymbol{\Phi}}^j]. \tag{7}$$

As stated in Castaings et al. (2002) and in the Introduction, evanescent modes do not carry energy. Their contribution though has to be accounted for in evaluating the energy balance to obtain an accurate scattering solution, as to satisfy the boundary conditions and guarantee energy conservation (undamped case).
The total energy is the sum of the energy of all reflected $E^{(j)}_{Refl}$ and transmitted $E^{(j)}_{Transm}$ modes, given an incident energy E_{in} amplitude equal to 1,

$$E_{in} = \sum_{j=1}^{N_M} (E^{(j)}_{Refl} + E^{(j)}_{Transm}). \tag{8}$$

Numerical investigations

In order to investigate the role of evanescent modes in the global-local method, a number of numerical analyses were run on defected aluminum and composite plates. For the aluminum plates, the values of the Poisson coefficient, density and Young modulus were: $\nu = 0.33$, $\rho = 2700\,kg/m^3$ and $E = 68\,GPa$, respectively. Composite plates had a 10-layers layup [0/ +45/ +90/ -45/ 0]$_S$ of T800/3900-2 Graphite/Epoxy unidirectional laminae, with a thickness of 0.2 mm for each layer. Material properties were those used in Liyong and Soutis (2003) and reported in Table 1 in the principal direction of material symmetry, where 1 is the fiber direction, 2 is the direction perpendicular to the fibers in the lamina plane, and 3 the through-thickness direction. The density of each lamina was $1550\,kg/m^3$.

The thickness of the plates was maintained fixed for all the tests, and equal to 2 mm. On the other hand, the geometry, size, and position of the defect vary inside the local zone, whose length was chosen equal to 5 mm for most of the examples, and greater than 5 mm in some cases.
Although the refinement of the finite element mesh is essential for numerical accuracy, the goal of this work was not to investigate this aspect. As such, the size of the finite

Table 1. Elastic properties of the composite lamina.

Property	C_{11}	C_{12}	C_{13}	C_{22}	C_{23}	C_{33}	C_{44}	C_{55}	C_{66}
GPa	162	3.98	3.98	10.4	3.81	10.4	3.45	6.21	6.21

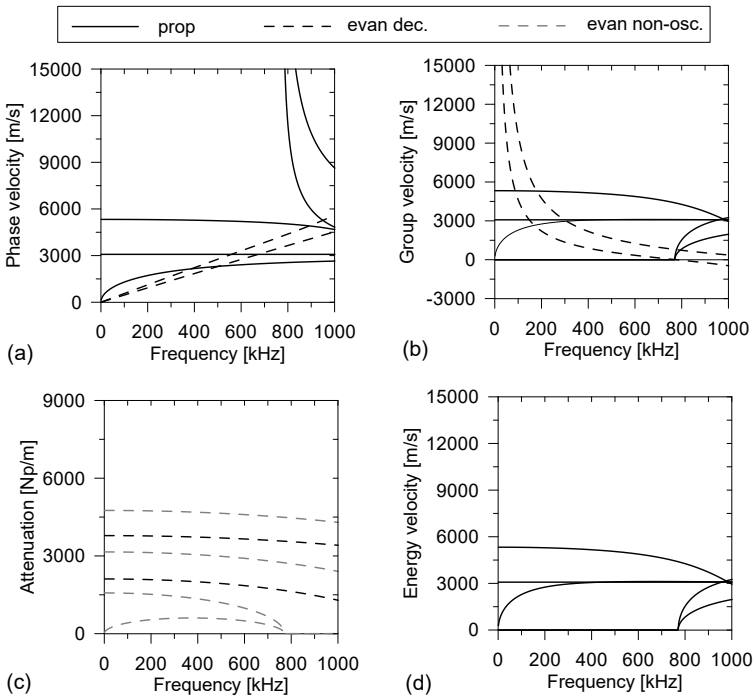

Figure 2. 2 mm thick aluminum plate dispersion and attenuation curves: a) phase velocity, b) group velocity, c) attenuation, d) energy velocity.

element was a parameter not investigated. It was considered sufficient to guarantee the presence of at least 20 elements for wavelength to reach acceptable numerical accuracy. In this way, each finite element was chosen linear (only four Gauss points) and squared, with sides equal to 0.1 mm.

The numerical code is the evolution of the Global-Local Matlab© code developed by Spada et al. (2020). The original 2D version of the code was enriched in order to include the effect of evanescent modes. It is known that evanescent modes are not able to carry energy. The energy flux carried by an evanescent mode through a cross-sectional area is null since the product of the terms within the square brackets in Eq. (7) results in a pure imaginary term. As a consequence, in the energy spectra the diagrams of the propagative modes only are visible. On the contrary, inclusion of evanescent modes in the Global-Local system completes the description of the physical problem, which is only approximated when the evanescent modes are absent. This fact is mathematically reflected in a better evaluation of the unknown coefficients leading to a more accurate estimation of the energy, thereby reducing the error in energy conservation.

At each frequency, the eigenvalue problem returns a number of evanescent modes. Not all evanescent modes need to be included in the analysis. Higher order evanescent modes usually have a negligible effect. As such, evanescent modes are included if $abs(Im(\xi h))$ is less or equal to a threshold value.

In this work, the sign of the energy velocity determines the traveling direction of propagating modes. For evanescent modes, instead, the traveling direction is obtained by the sign of the wavenumber: positive values of the real and imaginary parts referred to modes traveling in the positive direction.

Figures 2 and 3 show phase and group velocity dispersion curves, attenuation and energy velocity curves for aluminum and composite plates respectively, when the plate thickness is 2 mm and a threshold equal to 5 is chosen to select evanescent modes. For the aluminum plate, a total of 5 propagating modes (continuous lines in Fig. 2) and 6 evanescent modes (2 evanescent decaying modes and 4 evanescent non-oscillating end-modes, black and grey dotted lines in Fig. 2 respectively) were obtained in the DC-1 MHz frequency range. For the composite plate, a total of 5 propagating modes (continuous lines in Fig. 3) and 13 evanescent modes (2 evanescent decaying modes and 11 evanescent non-oscillating end-modes, black and grey dotted lines in Fig. 3 respectively) were obtained in the DC-500 kHz frequency range. In both figures, the higher order symmetric and anti-symmetric propagating modes are non-oscillating before their cut-on frequency.

In Figure 4 the results of the aluminum plate in the presence of a 2×1 mm centered rectangular defect are reported. Results correspond to an A0 incoming mode. The comparison is made between a local zone (LZ) size equal to 6 mm (minimum distance between the LZ boundary

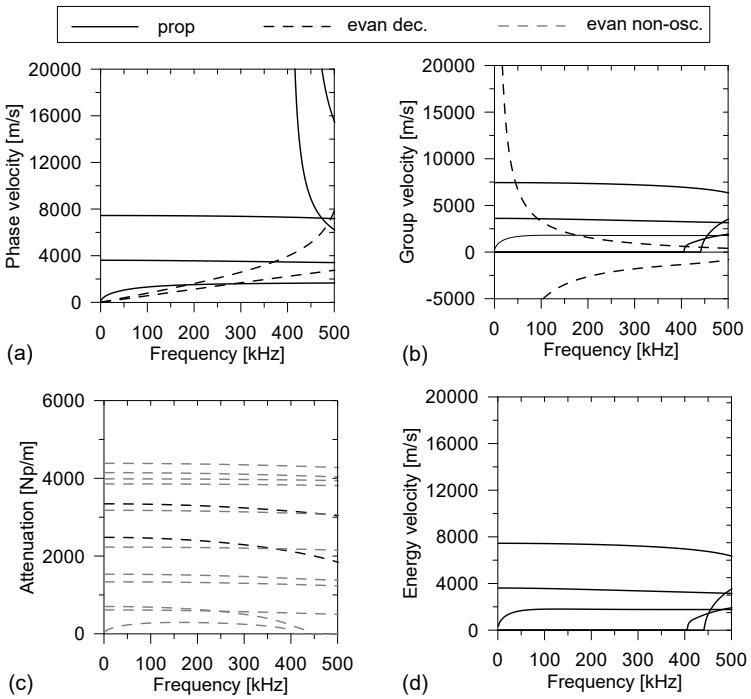

Figure 3. 2 mm thick composite plate dispersion and attenuation curves: a) phase velocity, b) group velocity, c) attenuation, d) energy velocity.

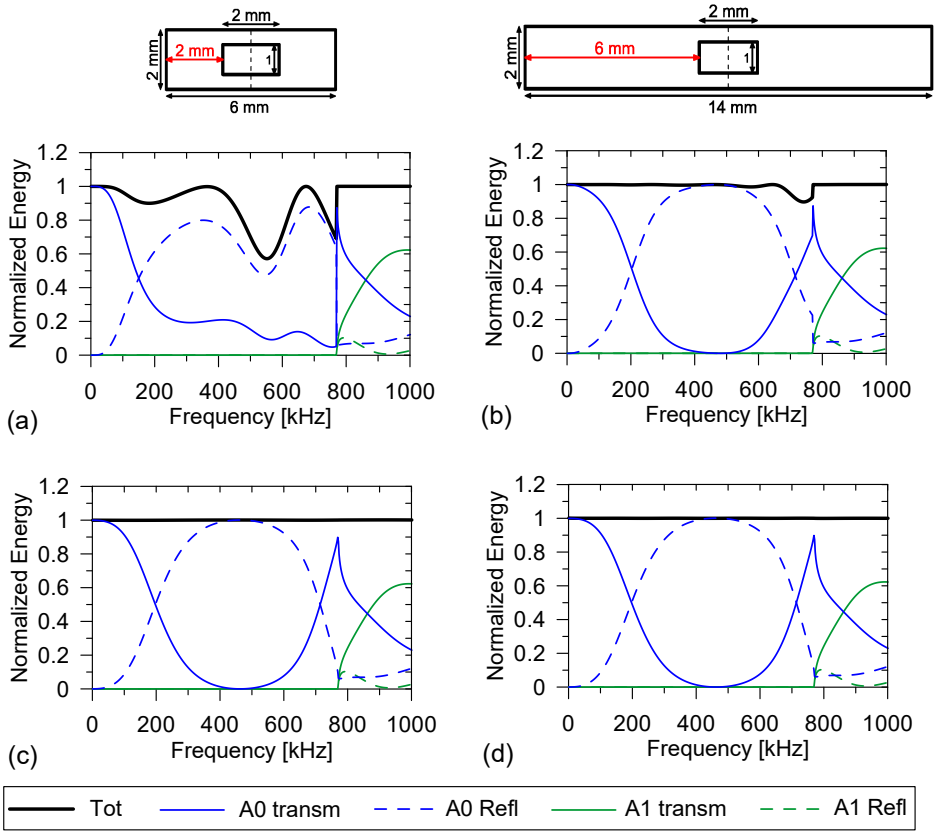

Figure 4. Aluminum plate. A0 incident energy spectra for a centered 2×1 mm rectangular defect having a distance of 2 mm (a, c) or 6 mm (b, d) from the left boundary: a, b) solutions without evanescent modes; c, d) solutions with evanescent modes.

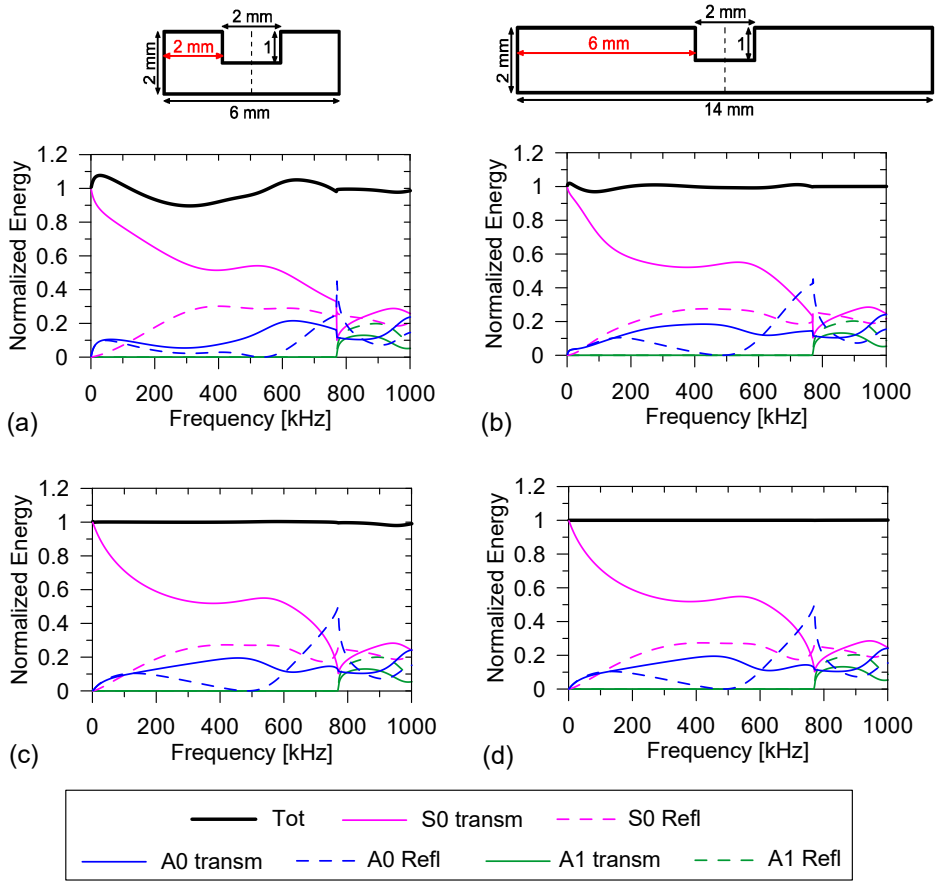

Figure 5. Aluminum plate. S0 incident energy spectra for a decentralized 2×1 mm rectangular defect having a distance of 2 mm (a, c) or 6 mm (b, d) from the left boundary: a, b) solutions without evanescent modes; c, d) solutions with evanescent modes.

and the defect of 2 mm, equivalent to the plate thickness, Figs. 4a-c) or 14 mm (minimum distance between the LZ boundary and the defect of 6 mm, equivalent to three times the plate thickness, Figs. 4b-d). The comparison is also performed considering propagating modes only (Figs. 4a-b) or including all the evanescent modes (Figs. 4c-d). In Fig. 4a it is apparent that the total normalized energy suffers from a large error (up to 40%) until the cut-on frequency of the higher order modes (DC-771 kHz). The error is nullified in the same range if evanescent modes are included (Fig. 4c). In the 771-1000 kHz, instead, no issues are observed, even in the absence of evanescent modes. It seems that error vanishes when A1 and S1 modes are included into the analysis, in their evanescent form before the cut-on frequency, in their propagative form after the cut-on frequency. If the distance between the LZ boundary and the defect increases to a 'safety' distance, the effect of evanescent modes becomes less prominent and the propagating modes alone approximate almost all the energy (Fig. 4b). As can be seen from Figure 4b and Figures 4c-d, the scattered energy spectra of all the involved modes are almost identical, proving once again acceptable results for only propagating modes when a sufficient distance is maintained between the scatterer and the LZ boundary. On the contrary, by including the evanescent modes, the LZ size can be reduced to a minimum, with a significant saving from a computational point of view.

In the parametric analyses of Figure 8, it will be shown that a minimum distance has to be guaranteed even in the presence of evanescent modes, for the sake of avoiding rough numerical errors. When the LZ boundary is too close to the scatterer and only propagating modes are taken into account, the results may be totally misleading, as in Figure 4a.
Similar comments can be made if a S0 incoming mode impinges upon a 2×1 mm rectangular notch in the aluminum plate (Fig. 5). In this example, mode conversions also take place. The results are reported for the cases of LZ boundary/defect distance equal to 2 mm (Figs. 5a-c) or 6 mm (Figs. 5b-d), in the absence of evanescent modes (Figs. 5a-b) or in their presence (Figs. 5c-d). A 10% maximum error in the total normalized energy reduces to 3% when stepping from a 2 mm distance to a 6 mm distance, when propagating modes only are considered. The errors are almost nullified in the presence of evanescent modes. When a distance of 6 mm is considered together with propagating modes only (Fig. 5b), scattered spectra coincide with the correct ones (Fig. 5d). On the contrary, for a distance of 2 mm, energy spectra have similar general trends which locally differ from the correct ones (see for example the differences between S0 and A0 transmitted and reflected spectra of Figs. 5a-c in the DC-771 kHz frequency range).

The results in Figures 6 and 7 correspond to two tests on the 2 mm thick composite plate: in the first test (Fig. 6), an

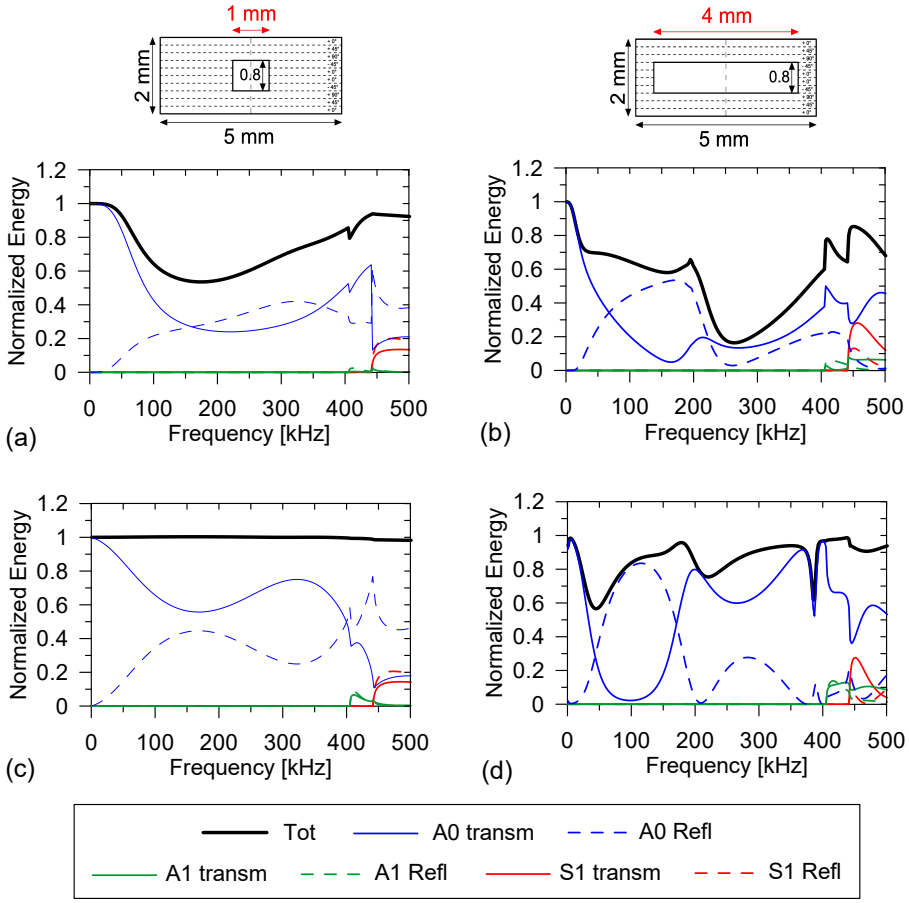

Figure 6. Composite plate. A0 incident energy spectra for a centered 1×0.8 mm (a, c) or 4×0.8 mm (b, d) rectangular defect (LZS= 5 mm): a, b) solutions without evanescent modes; c, d) solutions with evanescent modes.

A0 incident mode scattered on a centered rectangular defect; in the second test (Fig. 7), an S0 incident mode scattered on a rectangular notch. In these two tests the LZ size was maintained equal to 5 mm and the effects of varying defect sizes were analyzed.

The defect in Figures 6a-c has a rectangular shape of 1×0.8 mm with a 2 mm distance from the LZ boundary. In Figures 6b-d, the defect has a rectangular shape of 4×0.8 mm, with a distance from the LZ boundary equal to 0.5 mm. In both cases the defect involved the four central plies at 0 and -45 degrees. For a 1 mm long defect, the maximum error is 46% in the absence of evanescent modes, and less then 2% in the presence of evanescent modes (Fig. 6c). Scattered spectra are also different in the two cases in the DC-407 kHz frequency range. In the 407-500 kHz range some mode conversion into A1 and S1 modes occurs. The presence of evanescent modes, in particular, corrects the energy related to the scattered A1 mode. For a 4 mm long defect the maximum error is dramatically increased up to 80% in the absence of evanescent modes (Fig. 6b), and it still remains high (43%) if evanescent modes are included (Fig. 6d). This demonstrates that if the scatterer is too close to the boundary, the associated mathematical solution loses physical meaning also in the presence of evanescent modes. Scattered spectra significantly differ from one another and, as in the previous case, mode conversions taking place above 407 kHz are corrected by the inclusion of evanescent modes in the analysis.

The notch in Figure 7 has a rectangular shape with increasing dimensions, but a constant width/depth ratio of 2. In Figures 7a-c the defect has 0.4 mm and 0.2 mm long sides, with a distance LZ boundary/defect equal to 2.3 mm and a notch affecting the top 0 ply only. In Figures 7b-d the defect has 2 mm and 1 mm long sides, with a minimum distance LZ boundary/defect equal to 1.5 mm and a notch affecting the top five plies. The reflected S0 energy is higher as the depth of the notch increased, as expected. The incoming S0 mode is converted into transmitted and reflected A0 mode but the evaluation of the scattered A0 mode is incorrect in the absence of evanescent modes: Figure 7a and particularly Figure 7b show a numerical error in the total scattered energy, that is instead properly evaluated in Figures 7c-d. Also, the error is higher the closer the notch to the LZ boundary. The inclusion of evanescent modes reduces A0 mode conversion and corrects the overall solution.

In general, considering only propagating modes and comparing the cases of the composite plate with those of the aluminum plate, higher errors are expected in the composite due to the higher number of missing evanescent modes.

The absence of evanescent modes has two implications: it is

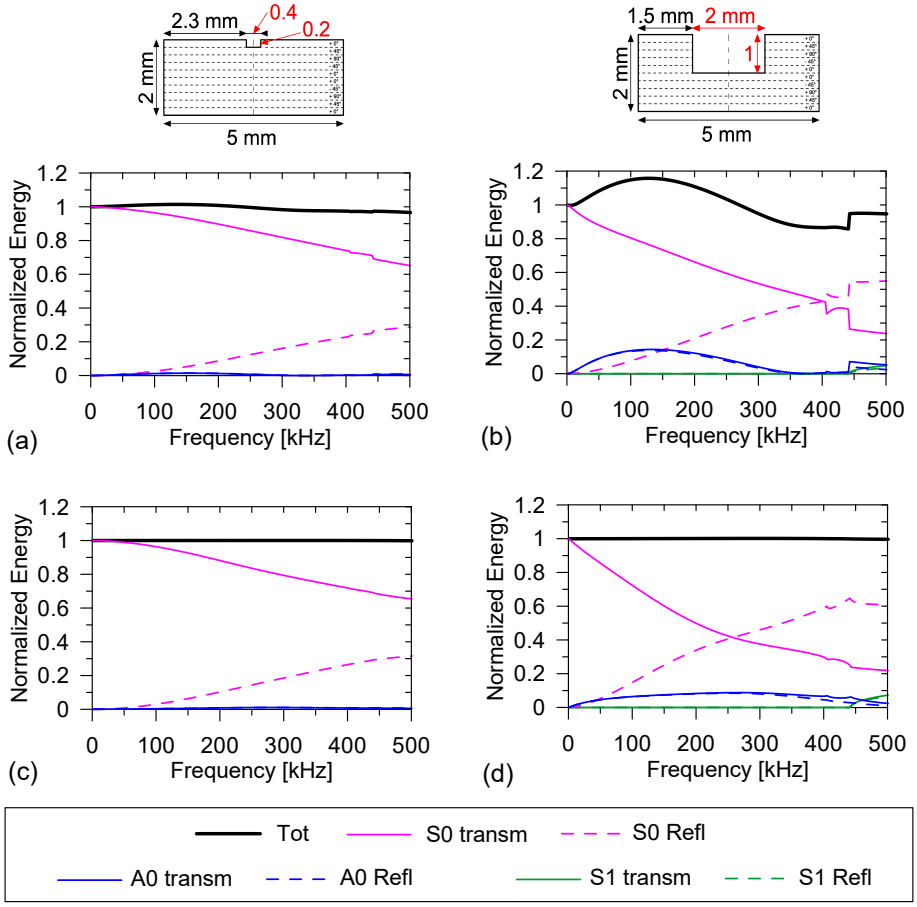

Figure 7. Composite plate. S0 incident energy spectra for a 0.4×0.2 mm (a, c) or 2×1 mm (b, d) rectangular notch (LZS= 5 mm): a, b) solutions without evanescent modes; c, d) solutions with evanescent modes.

necessary to always ensure a minimum LZ boundary/defect distance; error in the conservation of energy increases as the number of missing evanescent modes increases. The presence of evanescent modes, on the other hand, has two benefits: it improves the Global-Local numerical solution, and reduces to a minimum the length of the local zone, reducing computational costs, as well.

Discussion

In order to provide some rules of thumb, an intense parametric analysis was carried out for both the aluminum and composite plates, performing different tests by varying the LZ-scatterer relations. Results are reported in terms of the overall error in the total normalized energy. This error parameter is defined as the cumulative error over the entire frequency range, obtained by comparing the area under the numerical effective curve with the expected one:

$$Err = \sum_{k=1}^{n_f} \frac{|S_{num}^k - S_{exp}^k|}{S_{exp}^k} \tag{9}$$

where n_f is the total number of frequency steps, S_{num}^k is the effective observed numerical area under the total normalized energy curve and S_{exp}^k is the expected area.

Figure 8 and Table 2 summarize the results of the parametric analyses performed on the aluminum plate for the following cases:

1. LZ size equal to 5 mm with a centered square defect having side lengths ranging from 0.4 mm to 1.6 mm (Fig. 8a and Tab. 2a);
2. LZ size equal to 5 mm with a centered rectangular defect with an height of 1 mm and length ranging from 1 mm to 4 mm (Fig. 8b and Tab. 2b);
3. LZ size equal to 5 mm with a notch on the top. This notch has a rectangular shape with width/depth ratio equal to 2 and depth ranging from 0.2 mm to 1 mm (Fig. 8c and Tab. 2c);
4. LZ of different lengths with a rectangular notch on the top having width equal to 2 mm and depth equal to 1 mm. LZ boundary/notch distances range from 2 mm to 6 mm (Fig. 8d and Tab. 2d);
5. LZ of different lengths, with a centered square defect with sides equal to 1 mm. LZ boundary/notch distances range from 2 mm to 6 mm (Fig. 8e and Tab. 2e);
6. LZ size equal to 5 mm, with a not centered square defect with side equal to 1 mm and distances from the LZ boundary ranging from 0.5 mm to 2 mm (Fig. 8f and Tab. 2f).

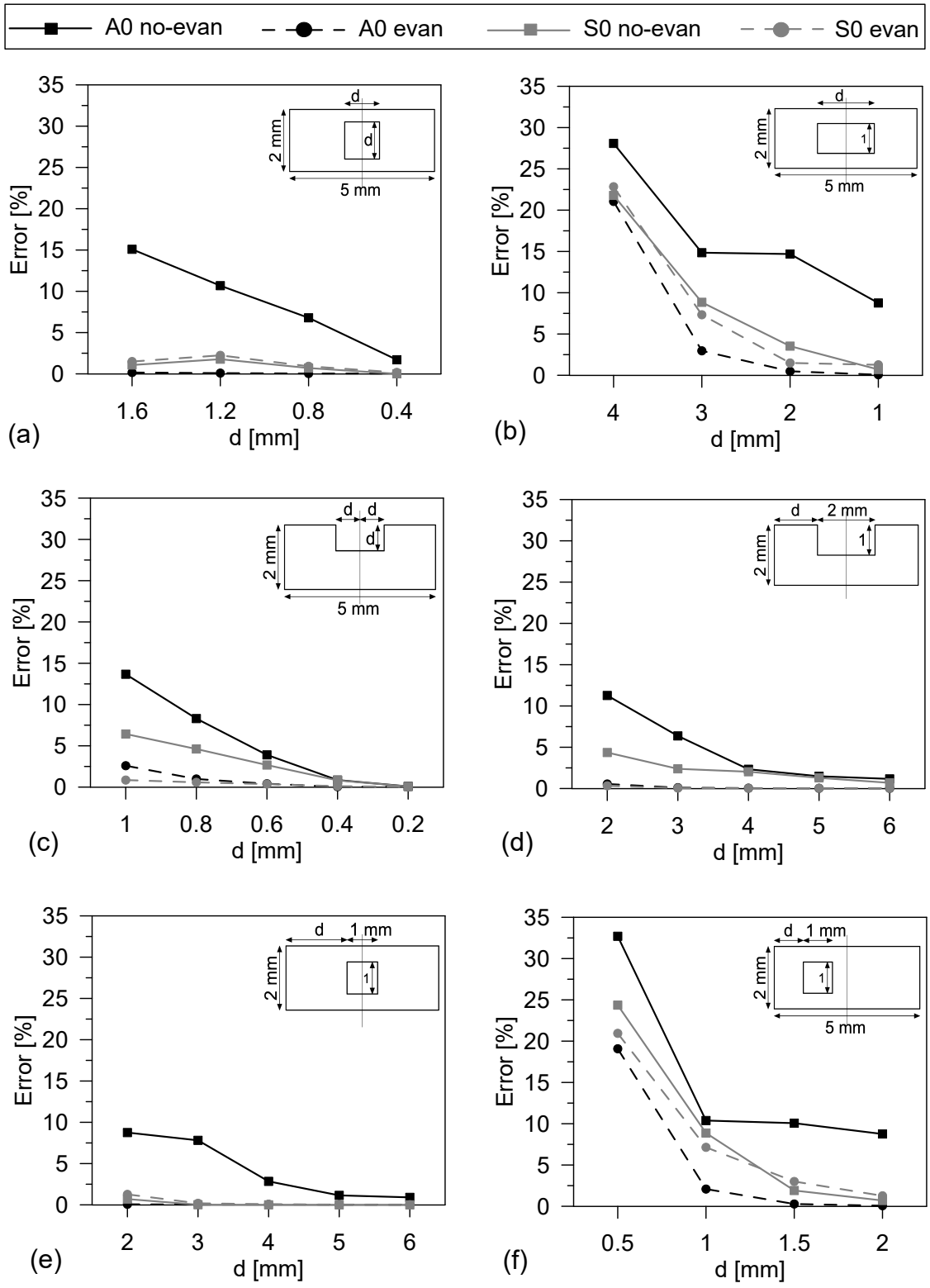

Figure 8. Aluminum plate. Parametric analysis in terms of total normalized energy error in the case of: a) centered square defect (LZS= 5 mm), b) centered rectangular defect (LZS= 5 mm), c) rectangular notch on the top (LZS= 5 mm), d) distance from the left boundary of a 2×1 mm rectangular notch (varying LZS), e) distance from the left boundary of a centered 1×1 mm defect (varying LZS), f) distance from the left boundary of a centered 1×1 mm defect (LZS= 5 mm).

In Figures 8 and 9 continuous lines refer to cases with propagating modes only, dotted lines refer to cases including the evanescent modes. Black lines refer to an A0 incoming mode, while gray lines refer to an S0 incoming mode. The parameter of interest is indicated as 'd'. In all the parametric studies it was assumed that the acceptable results were those

Table 2. Aluminum plate, Figure 8 data. Parametric analysis in terms of total normalized energy error in the case of: a) centered square defect (LZS= 5 mm), b) centered rectangular defect (LZS= 5 mm), c) rectangular notch on the top (LZS= 5 mm), d) distance from the left boundary of a 2×1 mm rectangular notch (varying LZS), e) distance from the left boundary of a centered 1×1 mm defect (varying LZS), f) distance from the left boundary and a not centered 1×1 mm defect (LZS= 5 mm).

a) Centered square defect dimensions - Fig. 8a

d [mm]	Error without evan [%]		Error with evan [%]	
	A0	S0	A0	S0
1.6	15.09	1.07	0.16	1.49
1.2	10.68	1.78	0.09	2.24
0.8	6.79	0.70	0.04	0.92
0.4	1.71	0.01	0.03	0.18

b) Centered rectangular defect width - Fig. 8b

d [mm]	Error without evan [%]		Error with evan [%]	
	A0	S0	A0	S0
4	28.08	21.79	21.05	22.84
3	14.85	8.84	2.96	7.33
2	14.69	3.53	0.49	1.49
1	8.75	0.70	0.07	1.27

c) Rectangular notch depth (width=2*depth) - Fig. 8c

d [mm]	Error without evan [%]		Error with evan [%]	
	A0	S0	A0	S0
1	13.67	6.43	2.59	0.85
0.8	8.30	4.61	0.98	0.58
0.6	3.90	2.67	0.40	0.36
0.4	0.85	0.81	0.05	0.11
0.2	0.08	0.07	0.04	0.03

d) LZ boundary/rectangular notch distance - Fig. 8d

d [mm]	Error without evan [%]		Error with evan [%]	
	A0	S0	A0	S0
2	11.27	4.36	0.55	0.33
3	6.37	2.39	0.10	0.05
4	2.33	2.03	0.04	0.02
5	1.49	1.29	0.03	0.03
6	1.17	0.69	0.03	0.02

e) LZ boundary/square defect distance Fig. 8e

d [mm]	Error without evan [%]		Error with evan [%]	
	A0	S0	A0	S0
2	8.75	0.70	0.07	1.27
3	7.81	0.02	0.03	0.19
4	2.84	0.00	0.04	0.07
5	1.15	0.00	0.03	0.01
6	0.91	0.00	0.03	0.01

f) LZ left boundary/0.8 mm square defect distance - Fig. 8f

d [mm]	Error without evan [%]		Error with evan [%]	
	A0	S0	A0	S0
0.5	32.70	24.36	19.08	20.94
1	10.38	8.87	2.09	7.14
1.5	10.07	1.91	0.28	3.00
2	8.75	0.70	0.07	1.27

where the global error was less than 2-3%. However, in the presence of propagating modes only, this threshold could be elevated to 5% for acceptable results.

A descending trend of error occurred in all cases as the d parameter changed from less to more favorable. Furthermore, higher error values were obtained for the A0 incoming mode with respect to the S0 incoming mode. In Figure 8a all the cases are almost acceptable, except for A0 mode without evanescent modes with d greater than 0.4 mm. Figure 8b shows that in the presence of a centered rectangular defect and an A0 incoming mode the results are not acceptable for all defect widths, when not considering evanescent modes. This means that in this case the results were not acceptable even when the LZ boundary/scatterer distance was at its maximum for the analyzed defect geometries (coincident with the plate thickness). For a S0 incoming mode without evanescent modes or when evanescent modes are included, the maximum allowable defect width was 2 mm. In Figure 8c, an acceptable d parameter is less than 0.8 mm, in the absence of evanescent modes; in the presence of an evanescent mode, the results are always acceptable, except for $d = 1$ mm and A0 incoming mode, for which they remain acceptable nonetheless. In the presence of a rectangular notch on the top of the plate (Fig. 8d) or a centered squared defect with 1 mm long side (Fig. 8e), without evanescent modes the minimum LZ boundary/scatterer distance should be at least 4 mm for A0 incoming mode, 2 mm for S0 incoming mode. Very good results were always obtained if evanescent modes were included. The case analyzed in Figure 8f is quite unusual, since the local zone is normally centered on the defect. However, it is presented here to investigate the influence of the LZ boundary scatterer distance, maintaining unchanged all other geometric parameters. The result shows that a distance of 2 mm is not sufficient for an A0 incoming mode using only propagating modes, while a distance of 1 mm can be considered sufficient if evanescent modes are included. A distance of 1.5 mm gives acceptable results for an incoming S0 mode in the absence of evanescent modes, which are otherwise unacceptable for a distance equal or below 1.5mm, even with evanescent modes.

These investigations were repeated for the composite plate, except for the last case. Table 3 reports the values of the errors obtained in each test, while the corresponding plots are depicted in Figure 9. In the absence of evanescent modes errors were in general higher than those obtained for the aluminum plate, but with an overall trend that can be regarded as equally descending when tuning the LZ to

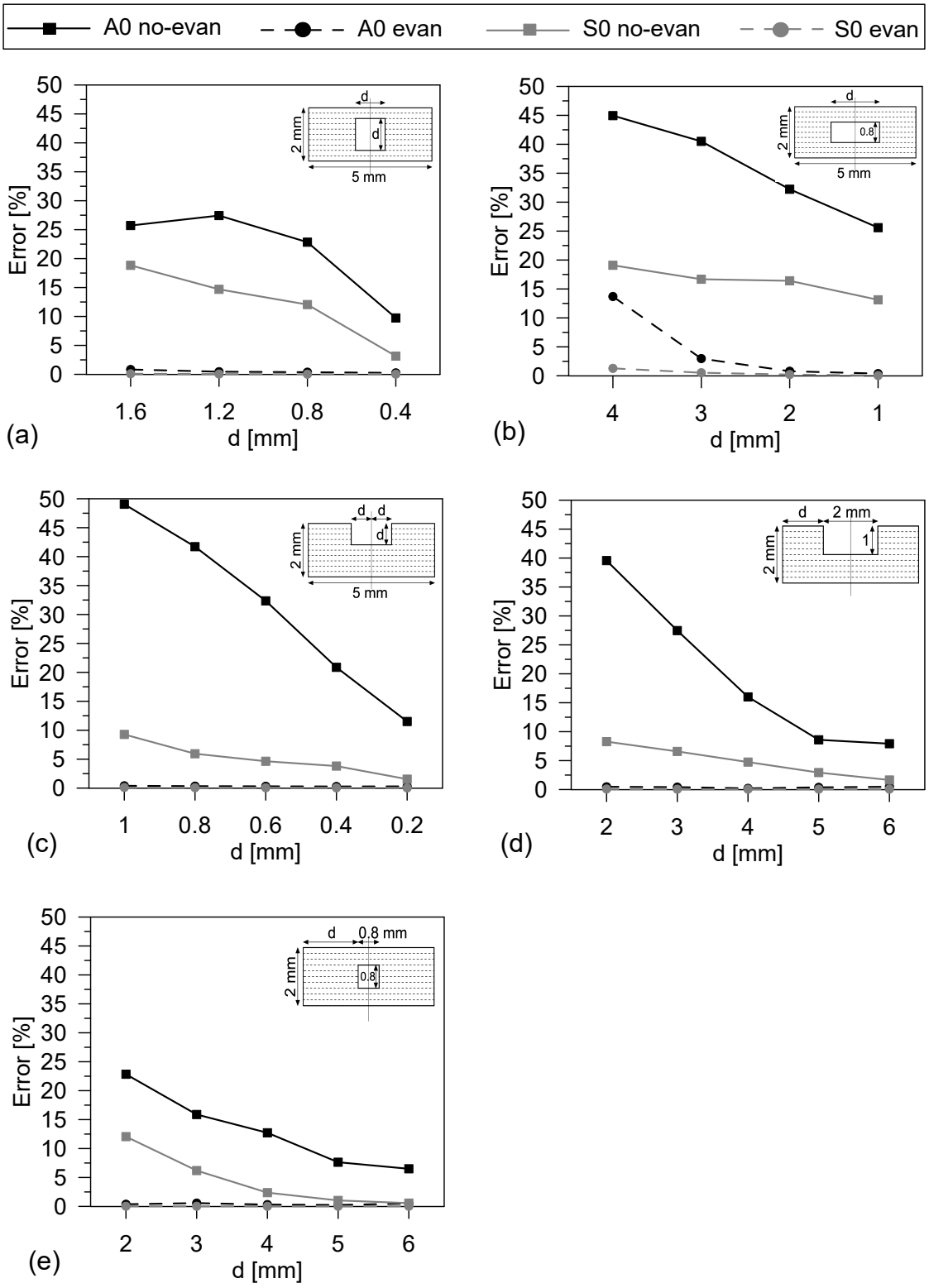

Figure 9. Composite plate. Parametric analysis in terms of total normalized energy error in the case of: a) centered square defect (LZS= 5 mm), b) centered rectangular defect (LZS= 5 mm), c) rectangular notch on the top (LZS= 5 mm), d) distance from the left boundary of a 2×1 mm rectangular notch (varying LZS), e) distance from the left boundary of a centered 0.8×0.8 mm defect (varying LZS).

scatterer dimension and/or including the evanescent modes. With an A0 incoming mode and only propagating modes included in the analysis the errors were always over the threshold. This demonstrates that a wider distance is required from the LZ boundary when the A0 mode is incoming. This is confirmed by the results shown in Figures 9d-e for a 2×1

mm rectangular notch or a 0.8 mm square defect with a distance of 6 mm from the LZ boundary, where the errors are nearly acceptable.

With a S0 incoming mode and no evanescent modes, a centered square defect case resulted as acceptable, if its side was no more than 0.4 mm long together with a LZ size equal to 5 mm (Fig. 9a); a centered $d \times 0.8$ mm rectangular defect was always not acceptable even if $d = 1$ mm (Fig. 9b); a rectangular notch with a width/depth ratio equal to 2 was acceptable if its depth was no more than 0.6 mm with LZ size of 5 mm (Fig. 9c) or if the distance from the boundary was at least 4 mm if the notch depth was 1 mm (Fig. 9d); a 0.8×0.8 mm centered square defect was acceptable if its distance from LZ boundary was at least 4 mm (Fig. 9e).
When evanescent modes were included, the only case showing not acceptable results was a 4×0.8 mm rectangular defect and A0 incoming (Fig. 9b), due to the very short distance from the LZ boundary. Acceptable results were found in the same case for an S0 incoming mode or for a 3×0.8 mm rectangular defect (Fig. 9b). For the rest of the analyzed cases very good results were obtained, always with an error less than 1%.
In summary, these results suggest that for an aluminum plate having a thickness of 2 mm, in the absence of evanescent modes the minimum LZ boundary/defect distance should be at least equal to 3 times the defect height and in any case not less than twice the plate thickness. When evanescent modes are included these values can be halved. For a composite plate having a thickness of 2 mm, in the absence of evanescent modes the minimum LZ boundary/defect distance should be greater than 6-8 times the defect height and in any case not less than 3-4 times the plate thickness. When evanescent modes are included these limits can be assumed to be the same as for aluminum.
To conclude the numerical investigations, two additional analyses were performed.
The first one was a repetition of the Figure 8b case for a $d = 4mm$, using a finer mesh where each finite element had a halved side, for a total number of elements 4 times the number of the previous discretization. For an A0 incoming mode the obtained errors were equal to 29.06% and 22.28% without or with evanescent modes respectively. For a S0 incoming mode the errors were equal to 21.83% and 23.10% without or with evanescent modes respectively. These results confirmed the values obtained with the previous finite element discretization, from which the initial assumptions regarding the finite element size can be considered valid.

The second analysis regarded an investigation on the ξh threshold on the centered 2×1 mm rectangular defect and a 2×0.8 mm rectangular defect for the aluminum and composite plates respectively, with a LZ size fixed to 5 mm. For the aluminum plate, if no evanescent modes were considered the error was equal to 14.64% and 3.53% for A0 and S0 incoming modes, respectively. Under the same conditions, for the composite plate, the errors were 32.23% and 16.41% for A0 and S0 incoming modes, respectively. Table 4 reports the trends of the errors by varying the ξh threshold, revealing that a threshold equal to 5 represents an optimal compromise. This value is in fact the one that ensures a total energy error of less than 2%, confirming other choices in the literature.

Concluding remarks.

In this paper the role of evanescent modes in Global-Local analyses of UGW in plates with varying local zone-scatterer relations has been investigated by improving a numerical code developed by the same authors in previous works. The performed studies can be considered at the base for guidelines on UGW scattering modelling.
All the studies provided energy spectra for A0, S0, or SH0 incident mode, in presence of centered rectangular or square defects, or rectangular notches. Both an aluminum and a composite case were analyzed. In this paper only the most significant cases were presented.
The effect of the evanescent modes has been studied by varying the distance of the region of interest from the defect scatterer. The region outside of the global-local boundary is considered far-field.
The main outcomes of the numerical analyses are here repeated. The most important outcome suggested by these analyses is that for an aluminum plate having a thickness of 2 mm, in the absence of evanescent modes, the minimum LZ boundary/defect distance should be at least equal to 3 times the defect height and in any case not less than twice the plate thickness. When evanescent modes are included these values can be halved. For a composite plate having a thickness of 2 mm, in the absence of evanescent modes the minimum LZ boundary/defect distance should be greater than 6-8 times the defect height and in any case not less than 3-4 times the plate thickness. When evanescent modes are included these limits can be assumed to be the same as for aluminum.
The absence of evanescent modes has two implications: it is necessary to always ensure a minimum LZ boundary/defect distance; error in the conservation of energy increases as the number of neglected evanescent modes increases. The presence of evanescent modes, on the other hand, has two benefits: it improves the Global-Local numerical solution, and it reduces to a minimum the length of the local zone, reducing computational costs, as well. If the LZ size guarantees a minimum distance between the boundary and the scatterer, only propagating modes are sufficient to provide a correct solution.
A study on the ξh threshold confirms that the value of 5 used in published works in the literature is the optimal compromise also for aluminum and composite plates.
Even if mesh effects have not been studied in depth, the performed test using a refined mesh confirmed that 20 finite linear elements per wavelength provide sufficiently accurate results.
The analyses revealed also localized effects in narrow frequency bandwidths due to internal resonances effects, particularly with respect to symmetric modes.
Future developments can be devoted to the best selection of specific evanescent modes in relation to different scatterer geometries and/or material properties and symmetries. Other efforts could involve experimental validations on forced Global-Local solutions employing evanescent modes.

Declaration of conflicting interests

The Authors declare that there are no conflicts of interests.

Table 3. Composite plate, Figure 9 data. Parametric analysis in terms of total normalized energy error in the case of: a) centered square defect (LZS= 5 mm), b) centered rectangular defect (LZS= 5 mm), c) rectangular notch on the top (LZS= 5 mm), d) distance from the left boundary of a 2×1 mm rectangular notch (varying LZS), e) distance from the left boundary of a centered 0.8×0.8 mm defect (varying LZS).

a) Centered square defect dimensions - Fig. 9a

d [mm]	Error without evan [%]		Error with evan [%]	
	A0	S0	A0	S0
1.6	25.72	18.84	0.83	0.10
1.2	27.44	14.69	0.46	0.05
0.8	22.84	12.06	0.37	0.03
0.4	9.75	3.15	0.25	0.03

b) Centered rectangular defect width - Fig. 9b

d [mm]	Error without evan [%]		Error with evan [%]	
	A0	S0	A0	S0
4	44.95	19.09	13.70	1.28
3	40.50	16.68	2.97	0.53
2	32.23	16.41	0.78	0.21
1	25.60	13.13	0.37	0.04

c) Rectangular notch depth (width=2*depth) - Fig. 9c

d [mm]	Error without evan [%]		Error with evan [%]	
	A0	S0	A0	S0
1	49.05	9.27	0.40	0.10
0.8	41.72	5.94	0.34	0.06
0.6	32.36	4.64	0.31	0.05
0.4	20.87	3.81	0.28	0.05
0.2	11.51	1.55	0.30	0.03

d) LZ boundary/rectangular notch distance - Fig. 9d

d [mm]	Error without evan [%]		Error with evan [%]	
	A0	S0	A0	S0
2	39.56	8.28	0.47	0.09
3	27.47	6.58	0.42	0.05
4	16.00	4.75	0.21	0.06
5	8.59	2.93	0.38	0.07
6	7.92	1.65	0.48	0.08

e) LZ boundary/square defect distance Fig. 9e

d [mm]	Error without evan [%]		Error with evan [%]	
	A0	S0	A0	S0
2	22.84	12.06	0.37	0.03
3	15.88	6.19	0.57	0.02
4	12.72	2.37	0.31	0.02
5	7.63	1.03	0.25	0.02
6	6.50	0.57	0.50	0.03

Table 4. n° of evanescent modes and errors by varying the selection threshold.

	Aluminum			Composite		
$abs(Im(\xi h))$	3	4	5	3	4	5
n° of evanescent modes	4	5	6	7	11	13
Error for A0 inc. mode [%]	0.19	0.49	0.49	1.78	0.88	0.78
Error for S0 inc. mode [%]	3.81	3.81	1.49	0.33	0.21	0.21

Funding

The authors received no financial support for the research, authorship, and/or publication of this article.

References

Bartoli I, Marzani A, di Scalea FL, Viola E (2006) Modeling wave propagation in damped waveguides of arbitrary cross-section. *Journal of Sound and Vibration*, 295(3–5), 685–707.

Benmeddour F, Treyssède F, Laguerre L (2011) Numerical modeling of guided wave interaction with non-axisymmetric cracks in elastic cylinders. *International journal of Solids and Structures*, 48(5), 764-774.

Castaings M, Le Clezio E, Hosten B (2002) Modal decomposition method for modeling the interaction of Lamb waves with cracks. *The Journal of the Acoustical Society of America*, 112(6), 2567-2582.

Diligent O, Lowe MJS, Le Clézio E, Castaings M, Hosten B (2003) Prediction and measurement of nonpropagating Lamb modes at the free end of a plate when the fundamental antisymmetric mode A0 is incident. *The Journal of the Acoustical Society of America*, 113(6), 3032-3042.

Frankforter E, Leckey C, Schneck III W (2019, May) Comparison of staggered grid finite difference schemes for ultrasound simulation in curving composites. In *AIP Conference Proceedings* (Vol. 2102, No. 1, p. 130002). AIP Publishing LLC.

Gavrić L (1995) Computation of propagative waves in free rail using a finite element technique. *Journal of Sound and Vibration*, 185(3), 531-543.

Gazis DC and Mindlin RD (1960) Extensional Vibrations and Waves in a Circular Disk and a Semi-Infinite Plate. *Journal of Applied Mechanics*, 27(3), 541–547.

Hayashi T, Song WJ, Rose JL (2003) Guided wave dispersion curves for a bar with an arbitrary cross-section, a rod and rail example. *Ultrasonics*, 41(3), 175–183.

Leckey CAC, Wheeler KR, Hafiychuk VN, Hafiychuk H, Timuçin DA (2018) Simulation of guided-wave ultrasound propagation in composite laminates: Benchmark comparisons of numerical codes and experiment. *Ultrasonics* (84): 187–200.

Lee BC, Staszewski WJ (2003) Modelling of Lamb waves for damage detection in metallic structures: Part I. Wave propagation. *Smart materials and structures*, 12(5), 804.

Liyong T, Soutis C (2003) *Recent Advances in Structural Joints and Repairs for Composite Materials*. Springer. ISBN: 978-94-017-0329-1

Mal A and Chang Z (2000) A semi-numerical method for elastic wave scattering calculations. *Geophysical Journal International*, 143(2), 328–334.

Marzani A, Viola E, Bartoli I, Di Scalea FL, Rizzo P (2008) A semi-analytical finite element formulation for modeling stress wave propagation in axisymmetric damped waveguides. *Journal of Sound and Vibration*, 318(3), 488-505.

Moreau L, Caleap M, Velichko A, Wilcox PD (2011) Scattering of guided waves by through-thickness cavities with irregular shapes. *Wave Motion*, 48(7), 586-602.

Ostachowicz W, Kudela P, Krawczuk M, Zak A (2011) *Guided waves in structures for SHM: the time-domain spectral element method*. John Wiley & Sons.

Poddar B and Giurgiutiu V (2016) Scattering of Lamb waves from a discontinuity: An improved analytical approach. *Wave Motion*, 65, 79–91.

Ricci F, Monaco E, Maio L, Boffa ND, Mal AK (2016) Guided waves in a stiffened composite laminate with a delamination. *Structural Health Monitoring*, 15(3), 351–358.

Ryue J, Thompson DJ, White PR, Thompson DR (2011) Wave reflection and transmission due to defects in infinite structural waveguides at high frequencies. Journal of *Sound and Vibration*, 330(8), 1737-1753.

Schaal C, Zhang S, Samajder H, Mal A (2017) An analytical study of the scattering of ultrasonic guided waves at a delamination-like discontinuity in a plate. *Proceedings of the Institution of Mechanical Engineers, Part C: Journal of Mechanical Engineering Science*, 231(16), 2947-2960.

Spada A, Capriotti M, Lanza di Scalea F (2020) Global-Local model for guided wave scattering problems with application to defect characterization in built-up composite structures. *International Journal of Solids and Structures*, 182, 267–280.

Spada A, Capriotti M, Lanza di Scalea F (2022) Global–local model for three-dimensional guided wave scattering with application to rail flaw detection. *Structural Health Monitoring*, 21(2), 370–386.

Srivastava A and Lanza di Scalea F (2010) Quantitative structural health monitoring by ultrasonic guided waves. *Journal of Engineering Mechanics*, 136(8), 937–944.

Staszewski WJ (2004) Structural health monitoring using guided ultrasonic waves. *Advances in smart technologies in structural engineering*. Springer. pp. 117–162.

Taweel H, Dong SB, Kazic M (2000) Wave reflection from the free end of a cylinder with an arbitrary cross-section. *International Journal of Solids and Structures*, 37(12), 1701-1726.

Willberg C, Duczek S, Vivar-Perez JM, Ahmad ZB (2015) Simulation methods for guided wave-based structural health monitoring: a review. *Applied Mechanics Reviews*, 67(1).

Zhou WJ and Ichchou MN (2011) Wave scattering by local defect in structural waveguide through wave finite element method. *Structural Health Monitoring*, 10(4), 335-349.